

# CellSymphony: Deciphering the molecular and phenotypic orchestration of cells with single-cell pathomics

Paul H. Acosta<sup>1,2,\*</sup> Pingjun Chen<sup>1,2</sup> Simon P. Castillo<sup>1,2</sup>  
 Maria Esther Salvatierra<sup>1</sup> Yinyin Yuan<sup>1,2,\*</sup> Xiaoxi Pan<sup>1,2,\*</sup>

<sup>1</sup>Translational Molecular Pathology Department, Division of Pathology and Laboratory Medicine,  
 The University of Texas MD Anderson Cancer Center, Houston, TX, United States

<sup>2</sup>Institute for Data Science in Oncology, The University of Texas MD Anderson Cancer Center, Houston, TX, United States

\*Corresponding authors: phacosta@mdanderson.org, yyuan6@mdanderson.org, xpan7@mdanderson.org

## Abstract

*Xenium, a new spatial transcriptomics platform, enables subcellular-resolution profiling of complex tumor tissues. Despite the rich morphological information in histology images, extracting robust cell-level features and integrating them with spatial transcriptomics data remains a critical challenge. We introduce CellSymphony, a flexible multimodal framework that leverages foundation model-derived embeddings from both Xenium transcriptomic profiles and histology images at true single-cell resolution. By learning joint representations that fuse spatial gene expression with morphological context, CellSymphony achieves accurate cell type annotation and uncovers distinct microenvironmental niches across three cancer types. This work highlights the potential of foundation models and multimodal fusion for deciphering the physiological and phenotypic orchestration of cells within complex tissue ecosystems.*

## 1. Introduction

The tumor microenvironment is a complex ecosystem where diverse cells spatially and molecularly interact, shaping cancer progression [2, 7]. Recent spatial transcriptomic advances enable high-resolution gene expression profiling, revealing tumor spatial organization and molecular heterogeneity [13, 15]. Among these technologies, the Xenium platform allows subcellular transcriptomic profiling of up to 5,000 genes, opening new avenues to investigate cell phenotypes, their communication, and the emerging tissue architecture [11].

Although histology images provide rich contextual and morphological information about cells and tissue structures, they lack molecular resolution. Conversely, Xenium offers molecular insights, but often struggles with accurate

cell classification in heterogeneous environments, particularly when cell boundaries are ambiguous or when expression profiles are sparse [17]. Hence, harnessing these two modalities results paramount to achieve a comprehensive understanding of cellular phenotypes in situ. Current methods often rely on indirect inference of genomic alterations [19] or marker gene-based [12] identification, which could be unreliable in complex tumor microenvironments. This highlights the necessity of integrating orthogonal modalities, histology and spatial transcriptomics, to improve tumor cell annotation. Several recent studies have sought to integrate histology images and spatial transcriptomics data, particularly from the Visium platform, to enhance downstream analyses such as gene imputation from morphology [8, 21, 22, 24], cell phenotyping [12, 25], and tissue characterization [4, 9, 10]. However, these efforts were mainly focused on spot-patch or spot-cell levels and did not fully exploit the rich, cell-level resolution. Consequently, the cell-level integration of histology and transcriptomics remains largely underexplored.

Foundation models have advanced both morphological [5, 23] and molecular analyses [6, 20]. Trained on extensive data across cancer types, these models learn generalizable representations that sharpen downstream tasks. Built on pathology and single-cell foundation models, UNI2 [5] and scGPT [6], we introduce **CellSymphony** (Fig. 1), a multimodal framework that integrates morphological and transcriptomic information at single-cell resolution to enhance spatial tissue characterization and derive biological insights into the highly orchestrated tumor ecosystem. Our experimental results demonstrate that integrating gene and morphological embeddings improves cell type annotation accuracy and enhances the discovery of spatial tissue subtypes and microenvironmental niches.

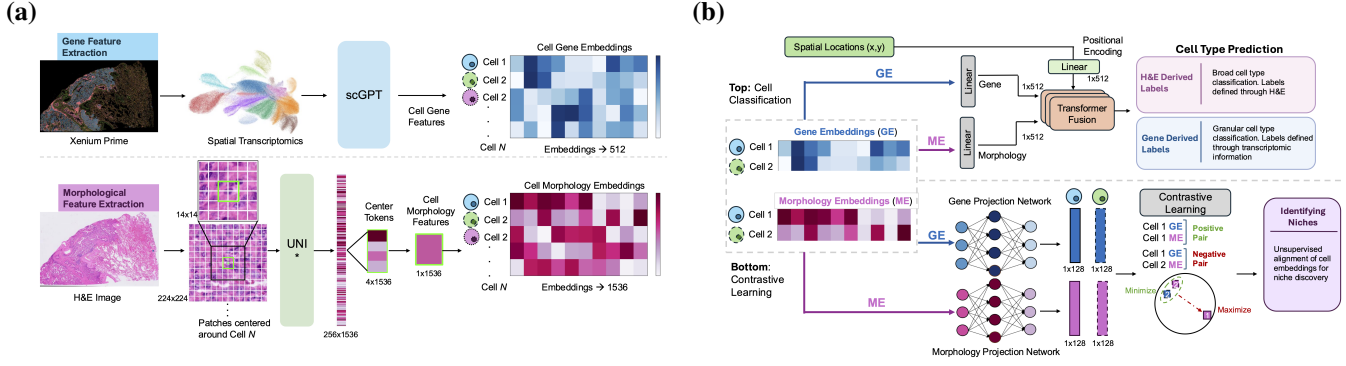


Figure 1. Overview of the CellSymphony framework. **(a)** Cell embeddings are derived from Xenium transcriptomes using scGPT (top) and from histology images via a modified UNI\* model (bottom). **(b)** Architectures of two deep learning approaches: transformer-based cell type annotation (top) and contrastive learning for cross-modal alignment of transcriptomic and morphological features (bottom).

## 2. Methods

Designed for Xenium Prime 5k spatial transcriptomics data paired with H&E images, the CellSymphony framework first extracts deep feature embeddings from each modality using foundation models. These embeddings then drive two core capabilities: (1) multimodal transformer-based cell type classification, and (2) contrastive learning to align morphology and transcriptomics.

### 2.1. Cell embedding at morphological and transcriptomic level

We derived a paired and modality-specific embedding for each cell (Fig. 1a). At the transcriptomic level, the cell’s gene counts vector is fed into the pre-trained scGPT model, producing a fixed transcriptomic embedding (Fig. 1a, Top). At the morphological level, a  $224 \times 224$  H&E patch ( $0.5\mu\text{m}/\text{px}$ ) centered on the same cell’s nucleus is passed through UNI2, generating the morphological embedding. Rather than using the model’s default tile feature representation, we extracted intermediate spatial tokens from UNI2 and aggregate those nearest the nucleus to generate a 1536-dimensional cell-specific morphology embedding, allowing flexible spatial context (Fig. 1a, Bottom). Together, these matched morphology and RNA vectors form the joint input for our cross-modal analyses.

### 2.2. Transformer-based cell type classification

We trained transformer-based models to classify cell types from gene expression and morphology embeddings derived from Xenium Prime data (Fig. 1b, Top). Cell annotations were sourced from either (1) SingleR [3], which uses reference-based transcriptomic classification, or (2) AI-sTIL [1, 18], an H&E-based segmentation and classification pipeline. Models were trained separately per label source, excluding ambiguous or low-confidence annota-

tions, and data was split into 80% training and 20% testing.

We evaluated four transformer architectures: (1) a **Uni-modal Transformer** trained on gene embeddings (GEB) alone; (2) a **Spatial Transformer** that adds a second input token for spatial coordinates using sinusoidal encoding; (3) a **Dual-Modality Transformer**, which processes gene and morphology embeddings (MEB) as separate input tokens, each tagged with a modality-specific token; and (4) a **Multi-Input Transformer**, which incorporates all three inputs (gene, morphology, spatial) using relative positional attention to guide interactions between tokens. Each embedding was projected into a shared dimensional space, then passed through a 6-layer transformer fusion encoder. The outputs were mean-pooled and classified using a linear head. All models were trained for 20 epochs using AdamW (learning rate  $3 \times 10^{-5}$ , batch size 64, weight decay 0.01), with cross-entropy loss and class weights to address label imbalance.

### 2.3. Contrastive learning representation between morphology and transcriptomics

To align the transcriptomic and morphological embeddings in a shared space, we implemented an unsupervised contrastive learning framework (Fig. 1b, Bottom). As described previously, cell-specific features were extracted from H&E and Xenium data using UNI2 and scGPT, respectively. Each modality was passed through a separate projection network to map into a 128-dimensional latent space.

The networks were trained using InfoNCE loss [16], which pulls matched embeddings (same cell) together while pushing unmatched pairs apart. Loss was computed bidirectionally, from morphology to transcriptomics and vice versa, on each batch of cells. Downstream analysis focused on the individual projections after training.

We evaluated the resulting features using UMAP [14], clustering, and spatial visualization to assess improvements

in the detection of biological signal and niches, particularly in morphology-derived representations.

### 3. Experiments and Results

#### 3.1. Dataset

We used lung ( $n_{\text{cells}} = 244,659$ ), breast ( $n_{\text{cells}} = 461,094$ ), and prostate ( $n_{\text{cells}} = 151,665$ ) *Xenium Prime 5k* datasets from 10x Genomics. Each sample includes gene expression from the Human Pan Tissue & Pathways panel, spatial cell coordinates, and matched high-resolution H&E images.

| Tissue   | $P_{\text{fib}}$ | $R_{\text{fib}}$ | $F1_{\text{fib}}$ | $P_{\text{lym}}$ | $R_{\text{lym}}$ | $F1_{\text{lym}}$ | $P_{\text{tum}}$ | $R_{\text{tum}}$ | $F1_{\text{tum}}$ |
|--|------------------|------------------|-------------------|------------------|------------------|-------------------|------------------|------------------|-------------------|
| <i>Unimodal Transformer (GEB Trained)</i>            |                  |                  |                   |                  |                  |                   |                  |                  |                   |
| Breast   | 0.71             | 0.65             | 0.68              | 0.55             | 0.65             | 0.60              | 0.85             | 0.85             | 0.85              |
| Lung   | 0.80             | 0.79             | 0.79              | 0.56             | 0.65             | 0.60              | 0.83             | 0.80             | 0.82              |
| Prostate   | 0.88             | 0.83             | 0.86              | 0.28             | 0.09             | 0.14              | 0.78             | 0.85             | 0.82              |
| <i>Spatial Transformer (GEB Trained)</i>             |                  |                  |                   |                  |                  |                   |                  |                  |                   |
| Breast   | 0.70             | 0.70             | 0.70              | 0.58             | 0.59             | 0.59              | 0.85             | 0.84             | 0.85              |
| Lung   | 0.79             | 0.82             | 0.81              | 0.56             | 0.63             | 0.59              | 0.87             | 0.79             | 0.82              |
| Prostate   | 0.88             | 0.85             | 0.86              | 0.31             | 0.09             | 0.14              | 0.80             | 0.85             | 0.82              |
| <i>Dual-Modality Transformer (GEB + MEB Trained)</i> |                  |                  |                   |                  |                  |                   |                  |                  |                   |
| Breast   | 0.90             | 0.90             | <b>0.90</b>       | 0.90             | 0.87             | <b>0.88</b>       | 0.92             | 0.95             | <b>0.93</b>       |
| Lung   | 0.90             | 0.93             | <b>0.91</b>       | 0.94             | 0.81             | <b>0.87</b>       | 0.91             | 0.91             | <b>0.91</b>       |
| Prostate   | 0.93             | 0.89             | <b>0.91</b>       | 0.71             | 0.66             | <b>0.68</b>       | 0.86             | 0.92             | <b>0.89</b>       |
| <i>Multi-Input Transformer (GEB + MEB Trained)</i>   |                  |                  |                   |                  |                  |                   |                  |                  |                   |
| Breast   | 0.93             | 0.85             | 0.89              | 0.84             | 0.93             | 0.88              | 0.92             | 0.95             | <b>0.93</b>       |
| Lung   | 0.93             | 0.87             | 0.90              | 0.77             | 0.96             | 0.85              | 0.90             | 0.92             | <b>0.91</b>       |
| Prostate   | 0.93             | 0.87             | 0.90              | 0.30             | 0.85             | 0.44              | 0.85             | 0.91             | 0.88              |

Table 1. Performance metrics for AI-sTIL predictions across tissues. **Abbreviations:** P = Precision, R = Recall, F1 = F1-score; fib = Fibroblast, lym = Lymphocyte, tum = Tumor.

#### 3.2. Performance of cell type classification

We evaluated classification models in three distinct tissue types: breast cancer, with large clusters of invasive and in situ carcinoma interspersed with normal ducts; lung cancer, where malignant epithelial cells are intermixed with stroma, immune cells, and tubular structures (e.g., bronchi); and prostate cancer, characterized by low immune infiltration and morphologically similar normal and cancerous glands.

Against morphology-based ground truth (AI-sTIL labels; Table 1), spatial encoding provided only a marginal improvement over the Unimodal Transformer. In contrast, the Dual-Modality Transformer, which integrated both gene expression and morphology, yielded the strongest performance. Adding spatial input via the (Multi-Input Transformer) did not deliver further gains, suggesting that once robust gene and morphology embeddings are in place, spatial information offers limited additional benefit to single cell annotation.

Using transcriptomic ground truth (SingleR; Table 2), the Dual-Modality Transformer consistently improved classification across cell types, achieving the highest F1 scores for B cells in lung (0.91), T cells in lung (0.94), and fibroblasts in prostate (0.86). Incorporating spatial context

(Multi-Input Transformer) further improved performance in lung—particularly for epithelial cells ( $F1 = 0.99$ ), B cells ( $F1 = 0.96$ ), T cells ( $F1 = 0.97$ ), and macrophages ( $F1 = 0.97$ ), highlighting the importance of spatial organization in this tissue. In contrast, spatial input had a limited impact in breast and prostate, where performance gains were modest or inconsistent. Notably, B cell classification in prostate dropped markedly ( $n = 313$ ), likely reflecting class imbalance or sensitivity to spatial noise.

#### 3.3. Enhancement of microenvironmental niche discovery through contrastive learning

While supervised classification achieved high accuracy, its reliance on predefined labels limits the discovery of nuanced biological structure. To overcome this, we applied a self-supervised contrastive learning framework to align gene expression and morphology into a shared space and evaluated the resulting morphology-derived projections.

Across tissues, contrast-trained morphology projections revealed refined spatial and phenotypic structure. In lung cancer, lymphocyte-rich niches became sharply defined, particularly in cluster 2, with improved spatial coherence and cleaner enrichment for B and T cells (Fig. 2a). In breast cancer, projections better delineated macrophage and fibroblast compartments and further stratified epithelial subtypes in multiple clusters (Fig. 2b). In prostate cancer, projections captured differentiation gradients among epithelial regions and provided clearer separation of glandular structures, aligning with known histological variation (Fig. 2c).

Together, these findings demonstrate that contrastive learning improves the ability of morphology-derived features to resolve complex tissue architecture, enabling unsupervised identification of immune-rich regions and tumor heterogeneity without requiring gene expression at inference.

### 4. Discussion and Conclusion

In this study, we introduced **CellSymphony**, a multimodal framework for integrating spatial transcriptomics and histological morphology at the single-cell level. Applied to Xenium Prime 5k data from lung, breast, and prostate cancer tissues, CellSymphony leverages multimodal fusion based on foundation models (scGPT and UNI2), empowering both supervised classification and contrastive learning.

A central strength of CellSymphony is its ability to operate at true single-cell resolution while flexibly fusing and aligning morphology and gene expression. The framework enables high classification performance across annotation sources (molecular-based SingleR and morphology-based AI-sTIL), and contrastive learning improves the biological structure captured by morphology alone—particularly in lymphocyte-rich and tumor epithelial regions.

| Tissue   | $P_{b,c}$ | $R_{b,c}$ | $F1_{b,c}$  | $P_{end}$ | $R_{end}$ | $F1_{end}$  | $P_{epi}$ | $R_{epi}$ | $F1_{epi}$  | $P_{fib}$ | $R_{fib}$ | $F1_{fib}$  | $P_{mac}$ | $R_{mac}$ | $F1_{mac}$  | $P_{t,c}$ | $R_{t,c}$ | $F1_{t,c}$  |
|--|-----------|-----------|-------------|-----------|-----------|-------------|-----------|-----------|-------------|-----------|-----------|-------------|-----------|-----------|-------------|-----------|-----------|-------------|
| <i>Unimodal Transformer (GEB Trained)</i>            |           |           |             |           |           |             |           |           |             |           |           |             |           |           |             |           |           |             |
| Breast   | 0.77      | 0.79      | 0.78        | 0.80      | 0.76      | 0.78        | 0.94      | 0.97      | 0.95        | 0.85      | 0.80      | 0.82        | 0.82      | 0.83      | 0.82        | 0.89      | 0.87      | 0.88        |
| Lung   | 0.94      | 0.87      | 0.90        | 0.94      | 0.93      | 0.94        | 0.97      | 0.97      | 0.97        | 0.93      | 0.92      | 0.92        | 0.88      | 0.95      | 0.92        | 0.93      | 0.94      | 0.93        |
| Prostate   | 0.54      | 0.55      | 0.55        | 0.84      | 0.76      | 0.80        | 0.92      | 0.97      | 0.94        | 0.89      | 0.85      | 0.87        | 0.89      | 0.80      | 0.84        | 0.84      | 0.77      | 0.81        |
| <i>Spatial Transformer (GEB Trained)</i>             |           |           |             |           |           |             |           |           |             |           |           |             |           |           |             |           |           |             |
| Breast   | 0.81      | 0.75      | 0.78        | 0.81      | 0.76      | 0.78        | 0.94      | 0.97      | 0.95        | 0.81      | 0.82      | 0.82        | 0.82      | 0.82      | 0.82        | 0.88      | 0.89      | 0.88        |
| Lung   | 0.88      | 0.92      | 0.90        | 0.94      | 0.93      | 0.93        | 0.97      | 0.98      | 0.97        | 0.92      | 0.93      | <b>0.93</b> | 0.93      | 0.93      | 0.93        | 0.94      | 0.92      | 0.93        |
| Prostate   | 0.76      | 0.49      | 0.59        | 0.88      | 0.75      | 0.81        | 0.93      | 0.96      | 0.95        | 0.88      | 0.87      | 0.88        | 0.80      | 0.85      | 0.82        | 0.84      | 0.79      | 0.81        |
| <i>Dual-Modality Transformer (GEB + MEB Trained)</i> |           |           |             |           |           |             |           |           |             |           |           |             |           |           |             |           |           |             |
| Breast   | 0.78      | 0.83      | <b>0.81</b> | 0.94      | 0.68      | <b>0.79</b> | 0.94      | 0.98      | <b>0.96</b> | 0.84      | 0.82      | <b>0.83</b> | 0.85      | 0.82      | <b>0.83</b> | 0.90      | 0.89      | <b>0.89</b> |
| Lung   | 0.91      | 0.92      | 0.91        | 0.95      | 0.92      | 0.94        | 0.97      | 0.98      | 0.97        | 0.94      | 0.91      | <b>0.93</b> | 0.91      | 0.94      | 0.93        | 0.93      | 0.95      | 0.94        |
| Prostate   | 0.78      | 0.49      | <b>0.60</b> | 0.94      | 0.74      | <b>0.83</b> | 0.92      | 0.98      | <b>0.95</b> | 0.91      | 0.88      | <b>0.89</b> | 0.90      | 0.82      | <b>0.86</b> | 0.88      | 0.76      | <b>0.82</b> |
| <i>Multi-Input Transformer (GEB + MEB Trained)</i>   |           |           |             |           |           |             |           |           |             |           |           |             |           |           |             |           |           |             |
| Breast   | 0.78      | 0.82      | 0.80        | 0.69      | 0.82      | 0.75        | 0.97      | 0.95      | <b>0.96</b> | 0.79      | 0.84      | 0.82        | 0.79      | 0.86      | 0.82        | 0.93      | 0.84      | 0.88        |
| Lung   | 0.95      | 0.97      | <b>0.96</b> | 0.98      | 0.98      | <b>0.98</b> | 1.00      | 0.99      | <b>0.99</b> | 0.92      | 0.95      | <b>0.93</b> | 0.96      | 0.98      | <b>0.97</b> | 0.98      | 0.97      | <b>0.97</b> |
| Prostate   | 0.21      | 0.74      | 0.32        | 0.82      | 0.77      | 0.79        | 0.95      | 0.93      | 0.94        | 0.94      | 0.83      | 0.88        | 0.74      | 0.85      | 0.79        | 0.81      | 0.76      | 0.78        |

Table 2. Performance metrics for SingleR predictions across tissues. **Abbreviations:** P = Precision, R = Recall, F1 = F1-score; subscripts: b\_c = B cell, end = Endothelial, epi = Epithelial, fib = Fibroblast, mac = Macrophage, t\_c = T cell. GEB: gene embeddings and MEB: morphological embeddings.

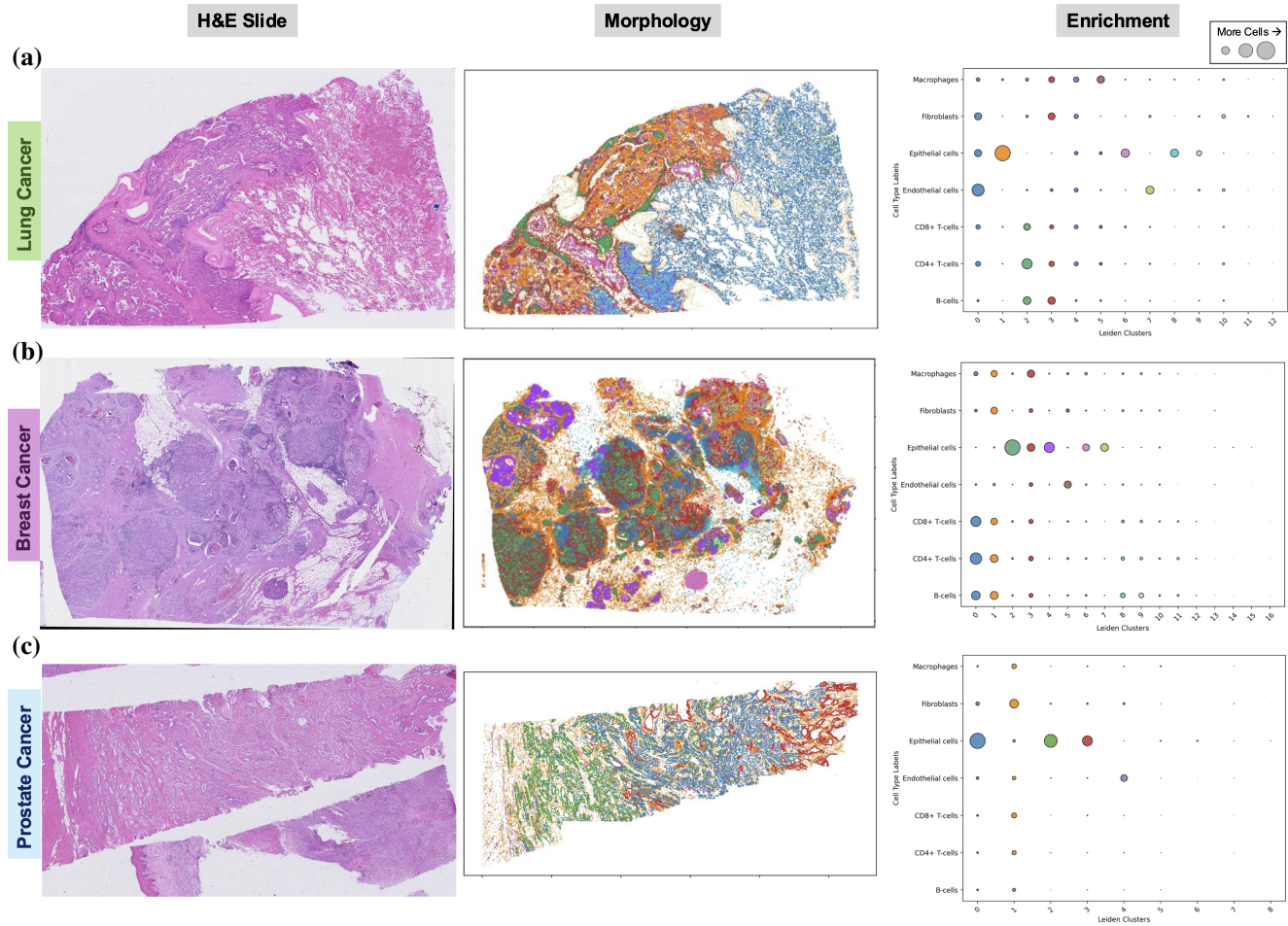


Figure 2. Morphology projection clustering after contrastive training for lung (a), breast (b) and prostate (c) samples. Each panel shows (from left to right): H&E image, the morphological patterns defined by each cluster, and the enrichment of cell classes within those clusters.



CellSymphony provides a flexible foundation for future multimodal spatial analyses. Its modular design enables incorporation of additional data types such as protein imaging or multiplexed RNA assays, and it can be adapted to incorporate spatial graphs or biological priors like gene ontology and regulatory networks. By aligning diverse modalities at single-cell resolution, CellSymphony opens new directions for investigating the tumor microenvironment and spatial cellular organization.

## References

- [1] Khalid AbdulJabbar, Shan E Ahmed Raza, Rachel Rosenthal, Mariam Jamal-Hanjani, Selvaraju Veeriah, Ayse Akarca, Tom Lund, David A Moore, Roberto Salgado, Maise Al Bakir, et al. Geospatial immune variability illuminates differential evolution of lung adenocarcinoma. *Nature medicine*, 26(7):1054–1062, 2020. [2](#)
- [2] Nicole M Anderson and M Celeste Simon. The tumor microenvironment. *Current biology*, 30(16):R921–R925, 2020. [1](#)
- [3] Dvir Aran, Agnieszka P Looney, Leqian Liu, Esther Wu, Valerie Fong, Austin Hsu, Suzanna Chak, Ram P Naikawadi, Paul J Wolters, Adam R Abate, et al. Reference-based analysis of lung single-cell sequencing reveals a transitional profibrotic macrophage. *Nature immunology*, 20(2):163–172, 2019. [2](#)
- [4] Feng Bao, Yue Deng, Sen Wan, Susan Q Shen, Bo Wang, Qionghai Dai, Steven J Altschuler, and Lani F Wu. Integrative spatial analysis of cell morphologies and transcriptional states with muse. *Nature biotechnology*, 40(8):1200–1209, 2022. [1](#)
- [5] Richard J Chen, Tong Ding, Ming Y Lu, Drew FK Williamson, Guillaume Jaume, Andrew H Song, Bowen Chen, Andrew Zhang, Daniel Shao, Muhammad Shaban, et al. Towards a general-purpose foundation model for computational pathology. *Nature Medicine*, 30(3):850–862, 2024. [1](#)
- [6] Haotian Cui, Chloe Wang, Hassaan Maan, Kuan Pang, Fengning Luo, Nan Duan, and Bo Wang. scgpt: toward building a foundation model for single-cell multi-omics using generative ai. *Nature Methods*, 21(8):1470–1480, 2024. [1](#)
- [7] Karin E De Visser and Johanna A Joyce. The evolving tumor microenvironment: From cancer initiation to metastatic outgrowth. *Cancer cell*, 41(3):374–403, 2023. [1](#)
- [8] Bryan He, Ludvig Bergenstr hle, Linnea Stenbeck, Abubakar Abid, Alma Andersson,  ke Borg, Jonas Maaskola, Joakim Lundeberg, and James Zou. Integrating spatial gene expression and breast tumour morphology via deep learning. *Nature biomedical engineering*, 4(8): 827–834, 2020. [1](#)
- [9] Siyu He, Yinyue Jin, Achille Nazaret, Lingting Shi, Xueer Chen, Sham Rampersaud, Bahawar S Dhillon, Izabella Valdez, Lauren E Friend, Joy Linyue Fan, et al. Starfish integrates spatial transcriptomic and histologic data to reveal heterogeneous tumor–immune hubs. *Nature Biotechnology*, 43(2):223–235, 2025. [1](#)
- [10] Jian Hu, Kyle Coleman, Daiwei Zhang, Edward B Lee, Humam Kadara, Linghua Wang, and Mingyao Li. Deciphering tumor ecosystems at super resolution from spatial transcriptomics with tesla. *Cell systems*, 14(5):404–417, 2023. [1](#)
- [11] Amanda Janesick, Robert Shelansky, Andrew D Gottscho, Florian Wagner, Stephen R Williams, Morgane Rouault, Ghezel Beliakoff, Carolyn A Morrison, Michelli F Oliveira, Jordan T Sicherman, et al. High resolution mapping of the tumor microenvironment using integrated single-cell, spatial and in situ analysis. *Nature communications*, 14(1):8353, 2023. [1](#)
- [12] Jiahui Jiang, Yunhe Liu, Jiangjiang Qin, Jianfeng Chen, Jingjing Wu, Melissa P Pizzi, Rossana Lazcano, Kohei Yamashita, Zhiyuan Xu, Guangsheng Pei, et al. Meti: deep profiling of tumor ecosystems by integrating cell morphology and spatial transcriptomics. *Nature communications*, 15(1):7312, 2024. [1](#)
- [13] ELHAM Karimi, N Simo, N Milet, W TE, A ALSH, ND QU, L AIL, R ABS, A ALIND, ND MORRIS GOODMA, et al. Method of the year 2024: spatial proteomics. *Nat Methods*, 21:2195–2196, 2024. [1](#)
- [14] Leland McInnes, John Healy, Nathaniel Saul, and Lukas Gro berger. Umap: Uniform manifold approximation and projection. *Journal of Open Source Software*, 3(29):861, 2018. [2](#)
- [15] Lambda Moses and Lior Pachter. Museum of spatial transcriptomics. *Nature methods*, 19(5):534–546, 2022. [1](#)
- [16] Aaron van den Oord, Yazhe Li, and Oriol Vinyals. Representation learning with contrastive predictive coding. *arXiv preprint arXiv:1807.03748*, 2018. [2](#)
- [17] Nejla Ozirmak Lermi, Max Molina Ayala, Sharia Hernandez, Wei Lu, Khaja Khan, Alejandra Serrano, Idania Lubo, Leticia Hamana, Katarzyna Tomczak, Sean Barnes, et al. Comparison of imaging-based single-cell resolution spatial transcriptomics profiling platforms using formalin-fixed, paraffin-embedded tumor samples. *bioRxiv*, pages 2024–12, 2024. [1](#)
- [18] Xiaoxi Pan, Maria E Salvatierra, Caner Ercan, Lakshmi Kakarala, Wei Lu, Ou Shi, Idania C Lubo Julio, Ignacio I Wistuba, Luisa M Solis Soto, and Yinyin Yuan. Tmeseg: Connecting histopathology with spatial transcriptomics through tumor microenvironment segmentation for lung cancer. *Cancer Research*, 85(8\_Supplement\_1):2426–2426, 2025. [2](#)
- [19] Beibei Ru, Jinlin Huang, Yu Zhang, Kenneth Aldape, and Peng Jiang. Estimation of cell lineages in tumors from spatial transcriptomics data. *Nature Communications*, 14(1): 568, 2023. [1](#)
- [20] Christina V Theodoris, Ling Xiao, Anant Chopra, Mark D Chaffin, Zeina R Al Sayed, Matthew C Hill, Helene Mantineo, Elizabeth M Brydon, Zexian Zeng, X Shirley Liu, et al. Transfer learning enables predictions in network biology. *Nature*, 618(7965):616–624, 2023. [1](#)
- [21] Hongyi Wang, Xiuju Du, Jing Liu, Shuyi Ouyang, Yen-Wei Chen, and Lanfen Lin. M2ost: Many-to-one regression for predicting spatial transcriptomics from digital pathology images. In *Proceedings of the AAAI Conference on Artificial Intelligence*, pages 7709–7717, 2025. [1](#)

- [22] Ronald Xie, Kuan Pang, Sai Chung, Catia Perciani, Sonya MacParland, Bo Wang, and Gary Bader. Spatially resolved gene expression prediction from histology images via bimodal contrastive learning. *Advances in Neural Information Processing Systems*, 36:70626–70637, 2023. [1](#)
- [23] Hanwen Xu, Naoto Usuyama, Jaspreet Bagga, Sheng Zhang, Rajesh Rao, Tristan Naumann, Cliff Wong, Zelalem Gero, Javier González, Yu Gu, et al. A whole-slide foundation model for digital pathology from real-world data. *Nature*, 630(8015):181–188, 2024. [1](#)
- [24] Daiwei Zhang, Amelia Schroeder, Hanying Yan, Haochen Yang, Jian Hu, Michelle YY Lee, Kyung S Cho, Katalin Susztak, George X Xu, Michael D Feldman, et al. Inferring super-resolution tissue architecture by integrating spatial transcriptomics with histology. *Nature biotechnology*, 42(9):1372–1377, 2024. [1](#)
- [25] Weiqin Zhao, Zhuo Liang, Xianjie Huang, Yuanhua Huang, and Lequan Yu. Hist2cell: Deciphering fine-grained cellular architectures from histology images. *bioRxiv*, pages 2024–02, 2024. [1](#)